ORIGINAL ARTICLE

On the infiltration of cellular solids by sheet molding compound: process simulation and experimental validation

Federico Bernardi[1] · Alberto Sensini[2,3] · Luca Raimondi[1] · Lorenzo Donati[1]

Abstract

This study examines a numerical method to simulate the production of novel multi-material metal-composite components, where an additive-manufactured cellular solid is infiltrated by a sheet molding compound (SMC) in a single-step compression molding operation. A single-fiber numerical approach is adopted to predict microstructural changes, such as fiber orientation, fiber-matrix separation, and fiber volume content variations during molding. The accuracy of the numerical predictions is confirmed by physical samples using micro-computed tomography and optical microscopy investigations at both the qualitative and quantitative scales. From optical microscopy observations, there emerged a positive correlation between experimental outcomes and simulation results, accurately capturing fiber swirling, wrinkling, and draping that occurred during molding. At a quantitative scale, a 0.6% mismatch was observed when void volume and unfilled areas were compared, as measured by micro-computed tomography and numerical simulation.

Keywords Carbon fibers · Microstructures · Process simulation · CT analysis · Out of autoclave processing

1 Introduction

The growing demand for lightweight multifunctional components with enhanced mechanical properties leads to the development of novel simulation tools combined with innovative monitoring techniques for time-to-market reduction and product certification. At the material level, there is a growing trend in the industry to combine fiber-reinforced plastics (FRPs) and metals to optimize the strength, weight, and durability of automotive and aerospace structures [1–3].

✉ Alberto Sensini
alberto.sensini@maastrichtuniversity.nl

✉ Luca Raimondi
luca.raimondi@unibo.it

1 DIN - Department of Industrial Engineering - Alma Mater Studiorum - Università di Bologna, Viale Risorgimento 2, 40136 Bologna, Italy

2 CTR Department, MERLN Institute for Technology-Inspired Regenerative Medicine, Maastricht University, Universiteitssingel 40, 6229 ER Maastricht, The Netherlands

3 cBITE Department, MERLN Institute for Technology-Inspired Regenerative Medicine, Maastricht University, Universiteitssingel 40, 6229 ER Maastricht, The Netherlands

In this context, FRPs are preferred over metals due to their greater structural efficiency, despite metals having better damage tolerance and high-temperature resistance and being less affected by exposure to solar radiation. Several deep interface anchoring technologies have been developed between metals and composite materials to take full advantage of the potential offered by the various material types [4–9]. These techniques involve sculpting the metal interface using additive or subtractive methods to create arrays of thin structures that protrude from the metal substrate. The wet composite substrate is then compressed onto the metal substrate, embedding the fine metal structure, and co-cured. The result is a multi-material hybrid joint that boasts improved structural performance due to the combined effect of adhesive and interlocking mechanisms generated at the interface between the different substrates. Although structural modeling of hybrid metal-composite joints has already been explored in the literature [4–6], the predictivity by numerical tools of process-induced defects such as fiber waviness [7, 10], fiber-matrix separation (FMS) [8], variation in fiber volume content (FVC), or void formation is scarcely documented [9]. Numerous authors have documented the negative impact of fiber misalignment in hybrid components within continuous FRP systems [11, 12]. Conversely, Raimondi et al. [13] have emphasized the significance of

evaluating fiber processing flow during the infiltration of a metallic lattice material by a sheet molding compound to mitigate the formation of voids and unfilled areas that can compromise joint strength. Although the reinforcement lengths may differ, the formation of these defects is governed by a common principle: the uncured polymer composite comprises fibers suspended in a viscous fluid matrix. The original prepreg distribution can be significantly modified during manufacturing by the FRP material flow and by interactions with metal structures. Analytical tools for describing fiber orientation evolution induced by the resin flow were developed starting from Jeffery's hydrodynamic model [13] by Folgar and Tucker and successors [14–17]. In these single-phase macroscopic models, the fibers are assumed to be rigid and to share the same velocity gradient experienced by the matrix flow [18]. Numerical implementations of those models are available in commercial codes such as Moldex 3D (CoreTech System Co., Ltd., Zhubei City, Taiwan) [19] or Moldflow (Autodesk, Inc., San Rafael, CA, USA) [20]. However, the reliability of these approaches is sensitive to fiber length and fails to account for FMS and local variation in fiber volume content (FVC) due to the simplification adopted [21]. Several single-fiber simulation approaches have been developed to overcome these limitations [22–27]. In single-fiber simulations, often referred to as direct fiber simulation (DFS), multiple rigid elements (particles, beams, or rigid rods) are flexibly connected to model the shape evolution of fibers inside the matrix flow. A commercially available tool that implements a velocity-base DFS model is 3D Timon Composite PRESS by Toray Engineering (Toray Engineering Solutions Co., Ltd., Shiga, Japan) [28]. Here, fibers are modeled as a chain of rigid rods connected by hinge spherical nodes, which allow the process simulation of prepregs with arbitrary fiber length. The hinge nodes receive velocity from a pre-computed fluid flow, allowing a one-way decoupled calculation of fiber bending during processing. On the other hand, several non-destructive techniques (NDTs) have been successfully employed to investigate the integrity of multi-material metal-composite components: ultrasound [29], thermography [30], and micro-computed X-ray tomography (microCT) [31]. microCT is particularly indicated to investigate, in a not disruptive way, the full-field morphology of samples of interest, acquiring information on their internal defects (such as porosity, void spaces, and variation in FVC) or the fiber distribution in FRP components. This study investigates the use of virtual process simulation to assess the development of composite microstructure and defect formation in the manufacturing of multi-material hybrid metal-composite components. The work focuses on the case where an SMC infiltrates a 3DP lattice material in one one-step compression molding operation. Fiber bending and orientation were considered in the numerical analysis for a reliable prediction of the forming process. Numerical results were benchmarked against physical samples at different scales through optical microscopy and microCT analysis to evaluate predictivity and accuracy. The comparison of numerical and experimental results showed a reasonable agreement.

2 Material and method

2.1 Physical sample preparation

The physical samples were two multi-material assemblies, each consisting of a 3D-printed metal part and an SMC part. Detailed definitions of geometries and process parameters are illustrated in a previous study by the authors [13] and reported here in short. The metal parts were crafted using two cylindrical AISI 316L stainless steel platforms as the base. A periodic network of 3D-printed pyramidal lattice material was grown on top of them, utilizing struts with a diameter of 0.8 [mm] created through the selective laser melting (SLM) technology. The unit cell measured 5 [mm] in height and had an edge base of 4.08 [mm], while the platform had a diameter of 99 [mm]. To produce the composite parts, two charges were created using a commercial HexMC®/C/2000/M77 prepreg composed of 50 [mm]-long strands supplied by Hexcel (Duxford, UK). One charge had strands randomly aligned with the molding direction (parallel configuration, see Fig. 1a), while the other had strands randomly aligned perpendicular to it (orthogonal configuration, see Fig. 1b).

To produce the parallel configuration charge, SMC strips measuring 35 [mm] in width were cut and then coiled into a roll with a 95-[mm] diameter. For the orthogonal configuration charge, 18 circular plies, each with a 95-[mm] diameter, were cut and stacked to create a 35-[mm] high charge. Both uncured SMC charges were positioned into the custom setup of Fig. 2a and molded using the processing parameters illustrated in Fig. 2b. The prepreg producer provided a range of suggested cure cycles. Samples were isothermally cured at 150 [°C] for 240 [s] under a pressure of 3 [MPa], mirroring the optimized industrial molding process for this material [32]. This cycle afforded ample time for positioning the charge, sealing the mold, ensuring consistent temperature, and achieving complete resin curing.

After molding, samples were sectioned orthogonally to the grid, as shown in Fig. 1c and d, to evaluate the interface microstructure visually.

2.2 Optical microscopy

The sectioned surfaces were conditioned by wet ground with 400, 800, and 2500 grit SiC paper. Care was taken in optimizing speed and pressure to avoid pullouts and artifacts.

Fig. 1 Experimental physical samples. **a**) charge for parallel configuration; **b**) View of orthogonal configuration charge; **c**) Frontal view of the sectioned zone for the parallel configuration; **d**) Frontal view of the sectioned zone for the orthogonal configuration
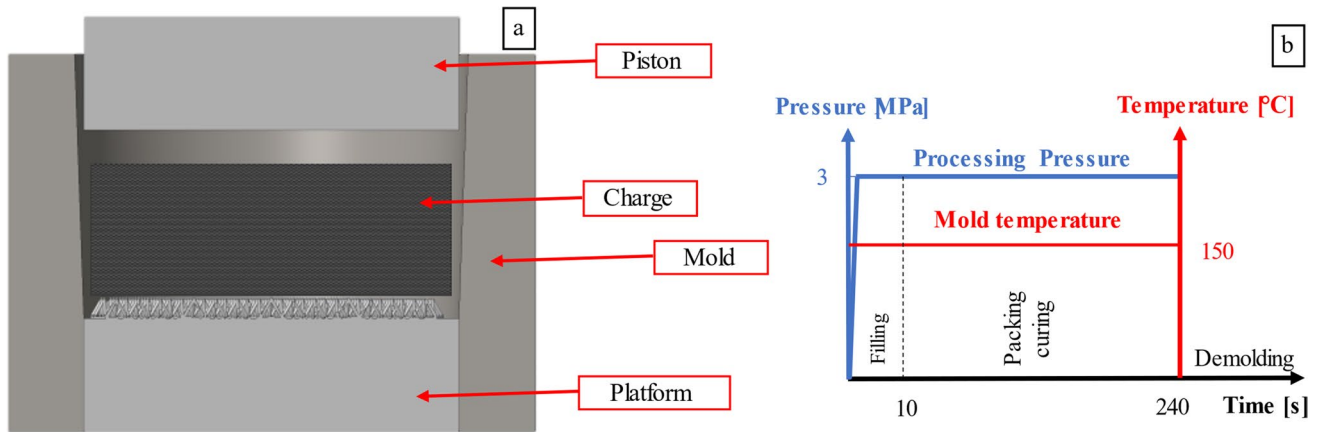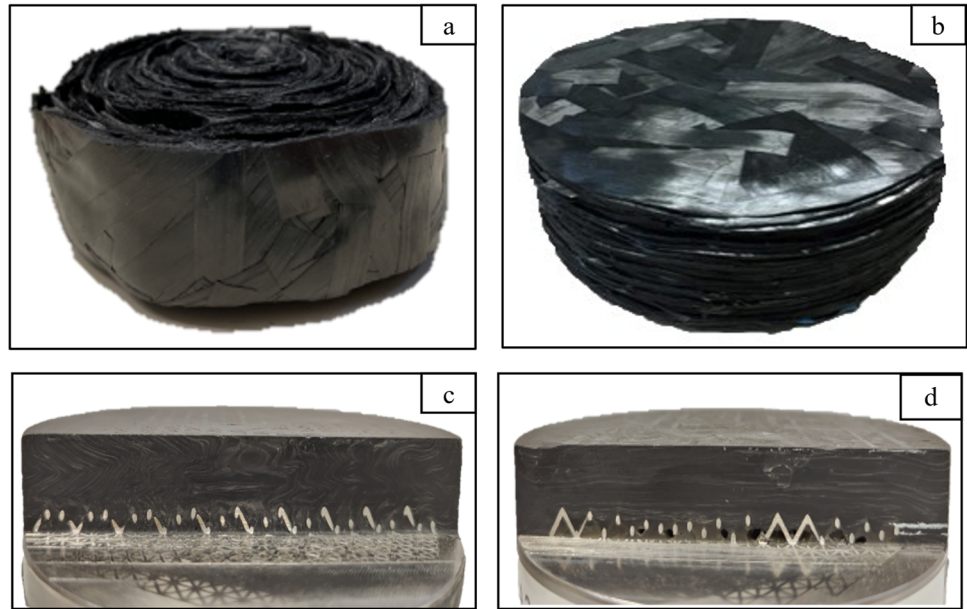
Fig. 2 Definition of experimental setup. **a**) layout of compression molding setup; **b**) Processing parameters used

Samples were studied in an optical ZEISS Stemi 508 Greenough Stereo Microscope at $5\times$ magnification. Digital micrographs were obtained by a ZEISS Axiocam 105 color camera with a 5-megapixel resolution and stitched into a full-width mosaic image by Microsoft Image Composite Editor [33].

2.3 microCT scan

Both multi-material assemblies were microCT scanned with a Diondo D7 High-Performance Linac CT System (Diondo GmbH, Hattingen, Germany) operated by Tec Eurolab Srl, Campogalliano, Italy.

The system is equipped with a high-energy Siemens SILAC® 6 MeV linear accelerator and a special, high-energy type detector with a resolution of 3000×3000 pixels. The samples were mounted on a rotating table between the X-ray source and detector (see Fig. 3) and imaged in "CtMode" with the following parameters: voltage $= 6$ [MeV], power $= 3.6$ [kW], current $= 600$ [µA], source frequency $= 600$ [Hz], achieving a voxel size of 120 [µm]. Projections were collected at rotational steps of 0.38° over 360°, with a total scanning time of 960 [s]. The scans were acquired and converted into 8-bit image stacks for post-processing. To ensure the quality of the output, all projections were processed by ImageJ [34] using a 3×3 median filter before reconstruction. Afterward, the open-source software MevisLab (Fraunhofer MEVIS, Bremen, Germany) was utilized to reconstruct and post-process each stack with precision and accuracy [35]. The micrographs in Sect. 2.2 were used to identify the characteristic grayscale ranges of values for each constituent of the multi-material assembly

Fig. 3 microCT measurement setup
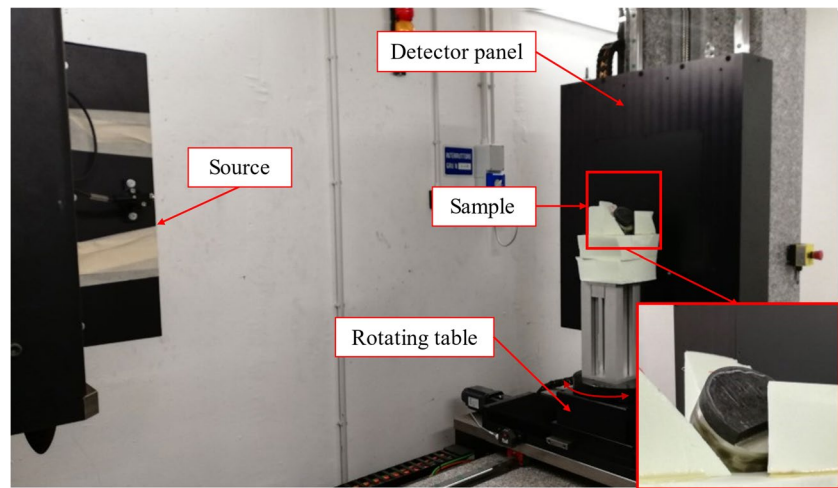
using the RegionGrowingMacro plugin of the software. The pixel grayscale ranges corresponding to air and resin were used to threshold and binarize the scans for a reliable measurement of their extent in both physical samples.

2.4 Governing equations and virtual process simulation

Flow analysis in a compression molding process is governed by the three primitive equations of traditional fluid dynamics: (i) the equation of continuity, (ii) the equation of motion, and (iii) the equation of energy. Solving these equations is impractical since calculations require considerable effort and computer resources [36]. Accordingly, in traditional 2.5D analysis, several authors have used the Hele-Shaw flow model to simplify the complex governing equation by ignoring the flow rate in the thickness direction. The potential flow assumption model of Eq. (1) was adopted in this work to overcome this limitation and realize a computationally efficient three-dimensional flow analysis model based on the hypothesis that the three components of the filling rate $\boldsymbol{u} = \{u, v, w\}$ are proportional to the pressure gradient in each of x, y, and z direction:

$$\begin{aligned} u &= -C_f(\eta, x)\frac{\partial P}{\partial x} \\ v &= -C_f(\eta, y)\frac{\partial P}{\partial y} \\ w &= -C_f(\eta, z)\frac{\partial P}{\partial z} \end{aligned} \quad (1)$$

where P is the forming pressure and C_f is flow conductance, which is defined as a function of viscosity η and position (x, y, z). The governing equation is thus given by Eq. (2):

$$\frac{\partial \rho}{\partial t} + \rho\left(C_f\frac{\partial P}{\partial x}\right) + \rho\left(C_f\frac{\partial P}{\partial y}\right) + \rho\left(C_f\frac{\partial P}{\partial z}\right) + \rho\frac{\partial h}{\partial t} = 0 \quad (2)$$

where ρ, C_f, h, P, and η denote the density, flow conductance, cavity height, forming pressure, and viscosity, respectively. The first term on the left side of the equation describes volumetric change by temperature and pressure, the second through fourth are responsible for viscosity flow, and the fifth describes the molded-in effect. The equation of energy governs the estimation of temperature evolution in the prepreg charge:

$$\rho c_v\left(\frac{\partial T}{\partial t} + u\frac{\partial T}{\partial x} + v\frac{\partial T}{\partial y} + w\frac{\partial T}{\partial z}\right) = \frac{\partial}{\partial x}\left(\lambda\frac{\partial T}{\partial x}\right) + \frac{\partial}{\partial y}\left(\lambda\frac{\partial T}{\partial y}\right)$$
$$+ \frac{\partial}{\partial z}\left(\lambda\frac{\partial T}{\partial z}\right) + \eta\dot{\gamma}^2 + \rho\frac{dQ}{dt} \quad (3)$$

where ρ is density; c_v is specific heat; u, v, and w are flow velocities of Eq. (1) in each direction; λ is thermal conductivity; η is viscosity; and $\dot{\gamma}$ is shear rate. The first term on the left side of the equation stands for temperature change; the second, third, and fourth terms are thermal advection. The first, second, and third terms on the right side signify thermal conductivity, the fourth shear heat generation, and the fifth one the heat generation rate caused by the exothermal reaction of prepreg while curing. The knowledge of prepreg viscosity and its evolution during the infiltration process is particularly relevant to accurately compute the velocity field of the charge as evidenced by Eq. (1), Eq. (2), and Eq. (3). In particular, the combination of the heating flow deriving from the hot surfaces of the tools and the heat generated by the exothermal reaction during cross-linking increases the viscosity as the degree of cure increases, controlling the deformability of the material. To describe these dependencies, three models are combined: the Arrhenius-like temperature-dependent Andrade model [34], the curing reaction rate-dependent Castro-Macosko model [37, 38], and the shear rate-dependent Cross model [39]. The combination of all three viscosity models extends the Castro-Macosko

model with a power law type shear rate dependence and leads to a modified Cross-Castro-Macosko model (Eq. (4)):

$$\eta(T, \alpha, \dot{\gamma}) = \frac{aexp\left(\frac{b}{T_0}\right)\left(\frac{\alpha_{gel}}{\alpha_{gel}-\alpha}\right)^{(D+E\alpha)}}{1+\left(\frac{a\,exp\left(\frac{b}{T_0}\right)\left(\frac{\alpha_{gel}}{\alpha_{gel}-\alpha}\right)^{(D+E\,\alpha)}}{\tau^*}\dot{\gamma}\right)^{(1-n)}} \qquad (4)$$

where T is the temperature; $\dot{\gamma}$ is the shear rate; α and α_{gel} are the degree of cure and the degree of cure at the gel point, respectively; a, b, and T_0 are coefficients from the Andrade model; D, E, and τ^* are coefficient from the Castro-Macosko model; and n is the power law index from the Cross model. Material input data for Eq. (4) are reported in Table 1 according to the experimental results of Teuwsen and co-workers [40] that characterized the same prepreg system used in this work.

The prepreg's degree of cure was calculated based on the differential scanning calorimetry (DSC) data shown in Fig. 4 (see Section S1 of Supplementary Information). As expected, the time to reach the maximum value became shorter as the heating rate increased. Equation (5) is used to express the cure reaction rate [41]:

$$\frac{d\alpha}{dt} = [A_1 exp(-\frac{E_1}{R \cdot T}) + A_2\ exp(-\frac{E_2}{R \cdot T})\alpha^m](1-\alpha)^n \qquad (5)$$

being $\frac{d\alpha}{dt}$ the reaction rate, i.e., the time derivative of the degree of cure α, A_1 and A_2 the pre-exponential factors, E_1 and E_2 the activation energies, T the reaction temperature while m and n are the overall reaction orders affected by temperature [42].

The reaction rate graphs shown in Fig. 4 can be fitted to Eq. (5), and the coefficients can be determined by the best fit for the measured quantities, as shown in Table 2.

Simulations were performed for parallel and orthogonal configurations using the Euler analysis method described in Eq. (1), Eq. (2), and Eq. (3) to express the complex 3D flow behavior experienced by the prepreg during infiltration through the commercial software 3D Timon 10 R8.1.1 CompositePRESS. Care was taken to optimize the mesh size
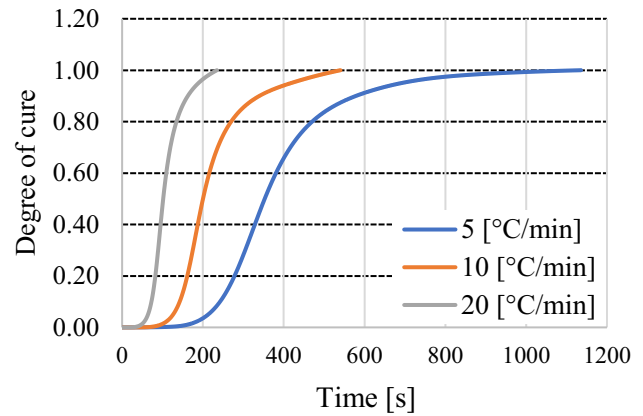

Fig. 4 Degree of cure with respect to time measured on three different heating ramps

to adequately capture the flow velocity field in the region surrounding the struts of the lattice material by extensive convergency studies. A voxel mesh with an edge length of 0.2 [mm] in the x-direction, 0.2 [mm] in the y-direction, and 0.15 [mm] in the Z-molding direction was found to be suitable for representing the molding cavity features. This work simulated a circular sector corresponding to one-eighth of the physical component to shorten the computation run time thanks to problem symmetry. Overall, this results in 1,081,114 mesh elements for the cavity. The fibers were modeled with a 50-[mm] length and 95 segments per fiber to describe bending accurately.

3 Results and discussion

3.1 microCT scans

The micrographic images of the parallel configuration were used to identify specific pixel grayscale values for segmenting the different materials of the metal-composite assembly using the RegionGrowingMacro function of MevisLab.

The same methodology was applied to the orthogonal configuration, which allowed for the identification of the void spaces under the lattices (pixel grayscale range, 20–64),

Table 1 Coefficients of mathematical models of Eq. (4) for HexMC®/C/2000/M77 prepreg

Constant	Value	Unit
a	$1.000 \cdot 10^{-11}$	[Pa · s]
b	$1.100 \cdot 10^4$	[°K]
D	$1.500 \cdot 10^1$	[−]
E	$-4.000 \cdot 10^0$	[−]
n	$6.000 \cdot 10^{-1}$	[−]
τ^*	$2.000 \cdot 10^2$	[Pa]
α_{gel}	$8.500 \cdot 10^{-1}$	[−]

**Table 2** Coefficients of the mathematical model of Eq. (5) for HexMC®/C/2000/M77 prepreg

Constant	Value	Unit
A_1	$1430 \bullet 10^{17}$	$[s^{-1}]$
A_2	$9.936 \bullet 10^{-2}$	$[s^{-1}]$
E_1/R	$1.925 \bullet 10^4$	[°K]
E_2/R	$8.795 \bullet 10^2$	[°K]
m	$9.353 \bullet 10^{-1}$	[−]
n	$1.306 \bullet 10^0$	[−]

regions where only resin was accumulated (pixel grayscale range, 65–74), the composite region (pixel grayscale range, 75–109), and the metal structure (pixel grayscale range, 110–255), as visible in Fig. 5. Although the grayscale ranges of resin and composite share similarities, an experimental cut-off value has been detected.

This could be attributed to the presence of inorganic fillers, which in turn contribute to varying the attenuation of X-ray radiation in the resin, thereby differentiating it from the composite material. The rendering of the segmented scans allowed the 3D reconstruction of both samples, as visible in Fig. 6a and d. The distinct differentiation between the metal and fibrous composite material becomes visually evident when restricting the reconstructions to correspond with the control volumes employed in the process simulations (Fig. 6b and e). In the parallel configuration, the

microCT measured a complete embedding of the metallic grid by composite material with no appreciable fiber matrix separation defects, as displayed in Fig. 6c. In contrast, diffuse unfilled regions characterized by resin-rich areas (blue regions, Fig. 6e, f) or voids (red regions, Fig. 6e, f) were identified and measured in the orthogonal configuration sample. A careful quantitative analysis revealed that these defects accounted for 29.3% of the composite volume. The challenge of non-destructively investigating the total volume of multi-material assemblies limits the ability to reduce voxel size, which hinders the discrimination of individual tows within the composite part. In order to properly visualize carbon fibers, which have an average diameter in the range of 6–8 μm, a minimum voxel size of 1.5 [μm] is required [43]. In turn, this deals with a maximum sample size of less than 4.5 [mm] for the microCT system used,

Fig. 5 Pixel grayscale levels identification by comparing micrography and microCT scans
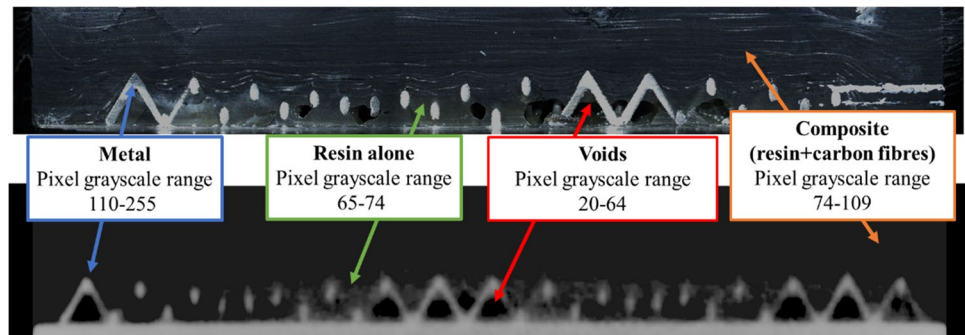
Fig. 6 3D rendering of the two multi-material assemblies: **a** parallel configuration; **b** control volume for parallel configuration; **c** control volume for parallel configuration without composite material; **d** orthogonal configuration; **e** control volume for orthogonal configuration; **f** control volume for orthogonal configuration without composite material
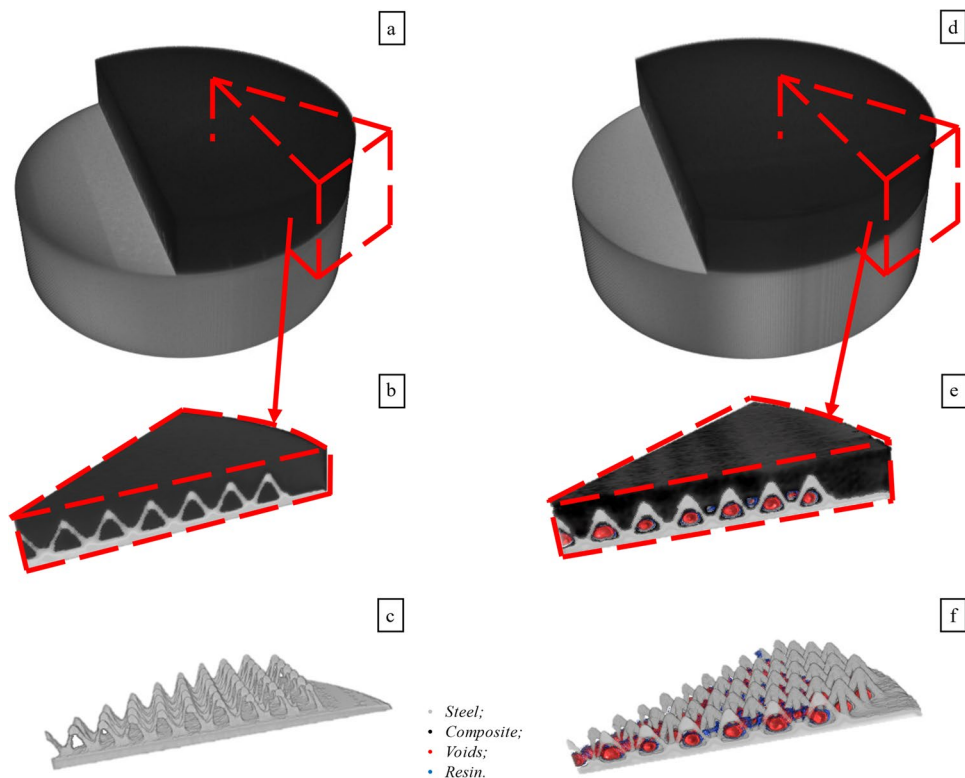
which is insufficiently small to characterize the extent of the defects found on the physical samples. On the metal side, no appreciable plastic deformation or buckling of the grid was detected in the scans for both configurations, as visible in Fig. 6c and f, respectively. Diameters of the metallic struts retrieved from microCT scans were found to be consistent (0.83 ± 0.07 [mm] for orthogonal configuration and 0.83 ± 0.09 [mm] for parallel configuration) with caliper measurements (0.82 ± 0.02 [mm]) in the entire reconstructed volume, thus confirming the quality of the thresholding procedure adopted in this work.

Moreover, these values, reporting a mean difference of 0.01 mm between the measurement of the diameter of the metallic struts obtained by the microCT scans and the ones obtained by using a caliper, confirm the high level of accuracy of the measurements.

3.2 Virtual process simulation

The high resolution achieved by the virtual process simulation enabled a detailed understanding of the infiltration evolution and defect formation within the composite part during processing. For both configurations, in a rapid initial transitory, the undeformed charges in Fig. 7a (parallel configuration) and Fig. 7d (orthogonal configuration) develop a predominantly radial flow that expands to fill the entire mold surface, with moderate movement along the vertical molding direction Z.

Afterward, the material flow proceeds with a parabolic profile up to the interaction with vertices of the lattice material. Here, different fiber/metal interaction mechanisms are computed depending on the original fiber distribution within the charge. For the parallel configuration (Fig. 7b), fibers are continuously deviated by the elements of the metal grid as their local distribution is significantly altered by a "wedge" effect induced by the shape of the repeating unit cell. Under the intense processing flow, deviated bent fibers are facilitated to penetrate the network in multiple directions and interact with other bundles, contributing to efficiently filling the lattice material. Notably, no significant fiber swirling or wrinkling is visible in the composite material charge at this stage. At the end of the infiltration process (Fig. 7c), a further bending of fibers due to the interaction with the base metal platform is markedly observable. From virtual process
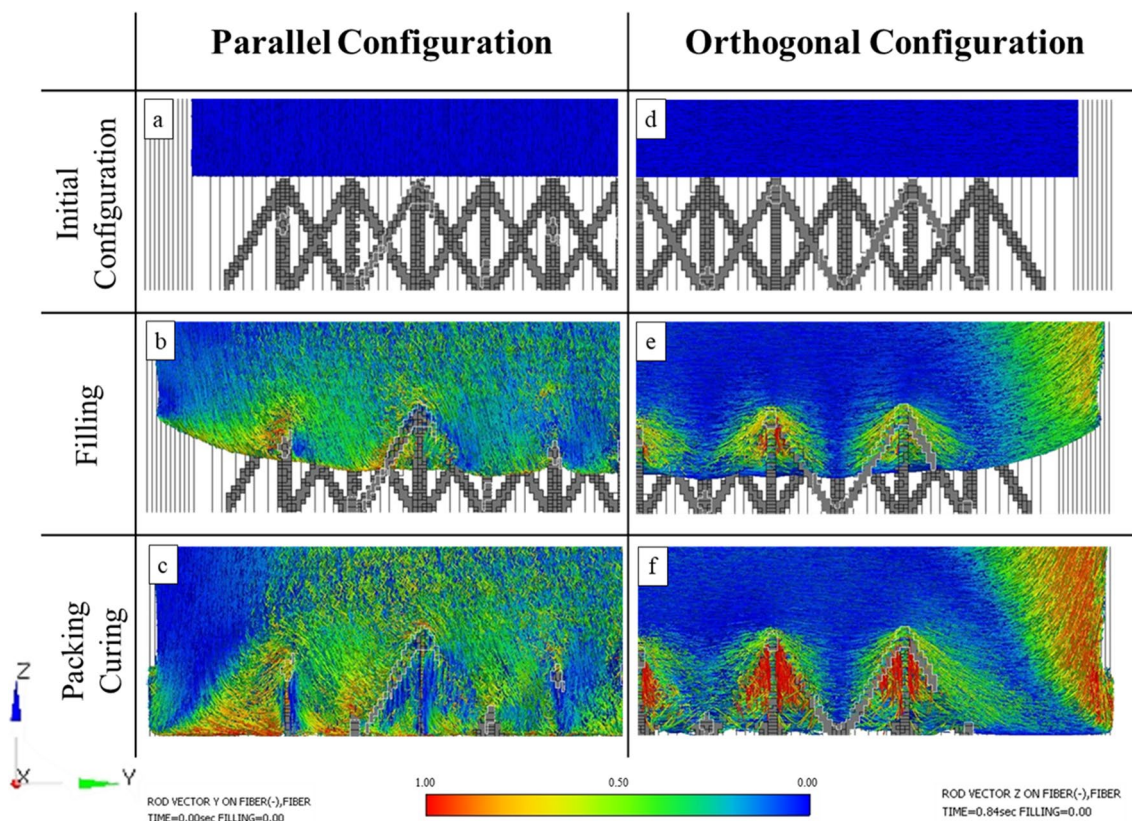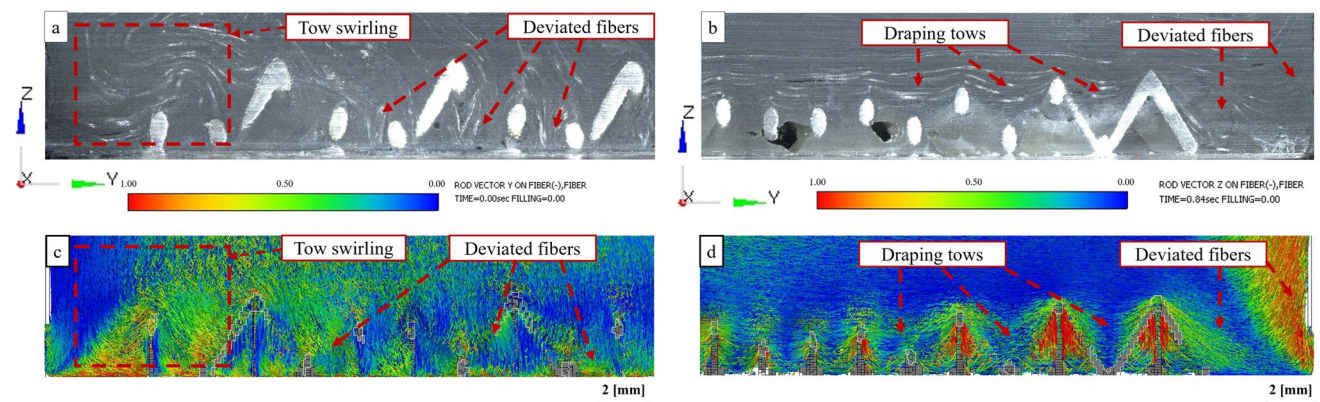

Fig. 7 Fiber deformation behavior according to the forming time: **a** parallel configuration at initial processing time; **b** parallel configuration at intermediate processing time; **c** parallel configuration at the end of the infiltration process; **d** orthogonal configuration at initial processing time; **e** orthogonal configuration at intermediate processing time; **f** orthogonal configuration at the end of the infiltration process

simulation results, it can be argued that fiber swirling and wrinkling observed in Raimondi et al. [13] are mainly generated in the latest stages of the infiltration process, as the composite material's viscosity is still too low to hinder the intense fiber motion. For the orthogonal configuration, a marked fiber deviation is achieved at the interface between the composite flow and the vertical surfaces of the mold, as visible in Fig. 7e. Interaction between the metallic grid and fibers from the FRP flow develops an incremental warpage of the pyramidal lattice material up to their base, as shown in Fig. 7f. No significant misalignment effect is visible in the charge's core for this configuration.
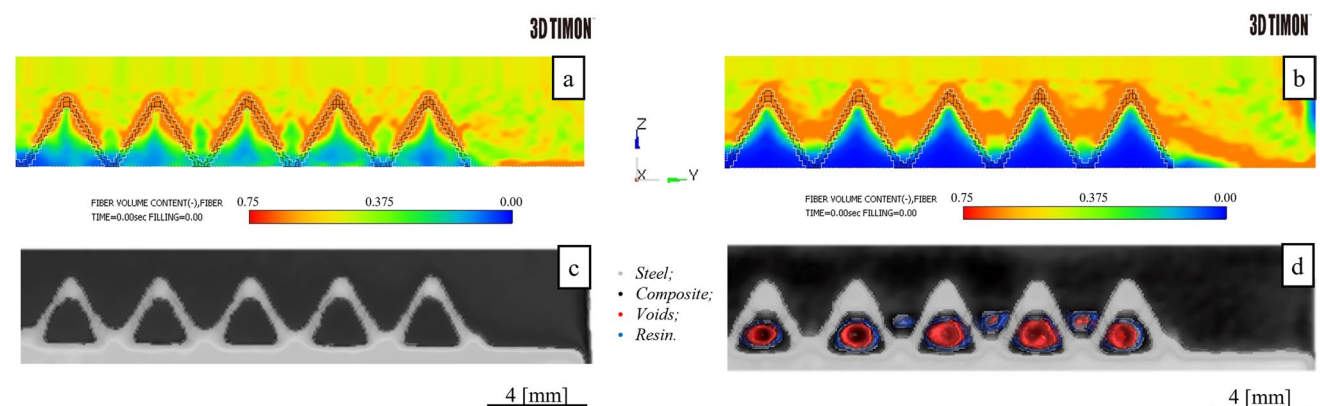
A comparison between DFS results and optical microscopy over sectioned regions of the multi-material component is reported in Fig. 8. In the physical sample for the parallel configuration (Fig. 8a), the fibers always managed to reach the base of the lattice structure and interact with it.

Qualitatively, the DFS model shown in Fig. 8c correctly captured the significant tow swirling experienced by the intense composite flow while interacting with the side mold surface. Moreover, the shape of the deviated fibers surrounding the lattice material and the base metal platform from simulation results appears to be qualitatively comparable to the experimental tow distribution of Fig. 8a. In contrast, the virtual process simulation results for the orthogonal configuration, shown in Fig. 8d, highlight the fibers' inability to penetrate the lattice material. This result agrees with the micrograph in Fig. 8b, where the draping of carbon fiber tow around the vertices of pyramidal lattice material is also markedly observable. A comparison between numerical results and microCT scans was performed to evaluate the approach's effectiveness, as displayed in Fig. 9. The computed FVC content for the parallel configuration, shown in Fig. 9a, is considerably greater than zero in the whole control volume.

Fig. 8 Comparison between DFS results and optical microscopy results. **a** DFS results for parallel configuration. **b** DFS results for orthogonal configuration. **c** Micrographic image of the sectioned region for parallel configuration. **d** Micrographic image of the sectioned region for orthogonal configuration

Fig. 9 Comparison between DFS results and microCT scans at the midplane of the control volumes. **a** DFS results for parallel configuration. **b** DFS results for orthogonal configuration. **c** microCT reconstruction for parallel configuration. **d** microCT reconstruction for orthogonal configuration

However, in this configuration, the computed FVC content is lower than the nominal 57% of the prepreg used in regions below the lattice network. At the same time, higher values are approached at the interface with the composite material and the inclined metallic struts.

Numerical results are consistent with the corresponding microCT reconstruction of Fig. 9c, where no voids or only-resin zones were detected in the composite part. As experimentally demonstrated in Raimondi et al. [13], this configuration has proven to provide the best performance in terms of mechanical strength and energy absorption, demonstrating the applicability of the technique to create a high-strength/high-toughness metal composite joint. In contrast, the numerical model of the orthogonal configuration, shown in Fig. 9b, predicts only zero values for fiber volume content under the metal grid. Moreover, it can be noticed that fiber volume content decreases rapidly to zero in the regions surrounding the bottom vertices of neighboring pyramids. It can be argued that FMS could cause this potential resin accumulation during processing flow, as the lattice grid significantly hinders the vertical flow of the fibers in this configuration. This hypothesis is further justified by the broader increase in fiber volume content in the regions surrounding the metal rods of the pyramidal lattice, where a maximum value of 60% for FVC is predicted. By comparing the numerical results with the microCT, Fig. 9d, it is possible to discriminate void (red regions) as well as only resin (blue regions) zones, all accounting for null fiber volume fraction. For the orthogonal configuration, regions with a fiber volume fraction close to zero constitute 28.7% of the simulated control volume, in excellent agreement with the 29.3% measured on microCT scans in Sect. 3.1, with a mismatch of 0.6%.

4 Conclusions

The possibility of reliably predicting the composite microstructure and defect formation during the infiltration process of cellular solids by SMC is demonstrated in this work. The implemented virtual process framework provided an exceptional platform for visualizing and comprehending the behavior of fibers during the manufacturing process, enabled a detailed representation of how fibers flowed, interacted with metallic grids, and contributed to eventually filling the lattice material. These visualizations provide a deeper understanding of the complex processes involved in creating multi-material assemblies, including enucleation and evolution of defects like FMS and the formation of voids due to insufficient filling. microCT analysis proved to be a reliable tool for non-destructively measuring the extent of those defects, accounting for 29.3% of the volume in the worst-case configuration. The acceptable mismatch of

0.6% between simulation and experimental data confirms the accuracy of the numerical methodology adopted in this paper. Fiber orientation predictions were qualitatively benchmarked by optical microscopy, further demonstrating the alignment of virtual simulation results with physical samples. Future research will focus on implementing robust standardization and calibration techniques for SMC substrates to overcome this limitation in synchrotron analysis. In future work, the result of the process simulation will be used to carry out a structural finite element analysis to correlate microstructural changes to interface mechanical properties. These analyses will also account for the internal stresses caused by the differing thermal expansion of the steel insert and FRP during curing.

Data availability The raw/processed data required to reproduce these findings cannot be shared at this time as the data also forms part of an ongoing study.

Declarations

Competing interests The authors declare no competing interests.

References

1. Crispo, L, Roper, SWK, Bohrer, R, Morin, R, Kim IY (2021) Multi-Material and Multi-Joint Topology Optimization for Lightweight

and Cost-Effective Design. Proceedings of the ASME 2021 International Design Engineering Technical Conferences and Computers and Information in Engineering Conference. Volume 3B: 47th Design Automation Conference (DAC). Virtual, Online. V03BT03A028. ASME. https://doi.org/10.1115/DETC2021-67317

2. Bader B, Türck E, Vietor T (2019) Multi material design. A current overview of the used potential in automotive industries. Technologies for Economical and Functional Lightweight Design; Springer: Berlin/Heidelberg, Germany, pp 3–13. https://doi.org/10.1007/978-3-662-58206-0_1

3. Gardiner G (2016) Is the BMW 7 Series the future of autocomposites. Composites World 7

4. Zhang H, Zhang L, Liu Z, Qi S, Zhu Y, Zhu P (2021) Numerical analysis of hybrid (bonded/bolted) FRP composite joints: A review. Compos Struct 262:113606. https://doi.org/10.1016/j.compstruct.2021.113606

5. Lambiase F, Scipioni SI, Lee C-J, Ko D-C, Liu F (2021) A state-of-the-art review on advanced joining processes for metal-composite and metal-polymer hybrid structures. Materials (Basel, Switzerland) 14. https://doi.org/10.3390/ma14081890

6. Nguyen ATT, Pichitdej N, Brandt M, Feih S, Orifici AC (2018) Failure modelling and characterisation for pin-reinforced metal-composite joints. Compos Struct 188:185–196. https://doi.org/10.1016/j.compstruct.2017.12.043

7. Nguyen NQ, Mehdikhani M, Straumit I, Gorbatikh L, Lessard L, Lomov SV (2018) Micro-CT measurement of fibre misalignment: application to carbon/epoxy laminates manufactured in autoclave and by vacuum assisted resin transfer moulding. Compos Part A Appl Sci Manuf 104:14–23. https://doi.org/10.1016/j.compositesa.2017.10.018

8. Hohberg M (2022) Experimental investigation and process simulation of the compression molding process of sheet molding compound (smc) with local reinforcements, Vol. 80. Karlsruhe: KIT Scientific Publishing. https://doi.org/10.5445/KSP/1000104914

9. Wang WW, Wang H, Wang HJ, Dong HY, Ke YL (2021) Microdamage initiation evaluation of z-pinned laminates based on a new three-dimension RVE model. Compos Struct 263: 113725. https://doi.org/10.1016/j.compstruct.2021.113725

10. Raimondi L, Tomesani L, Zucchelli A (2024) Enhancing the robustness of hybrid metal-composite connections through 3D printed micro penetrative anchors. Appl Compos Mater. https://doi.org/10.1007/s10443-024-10224-1

11. Inverarity SB, Das R, Mouritz AP (2022) Composite-to-metal joining using interference fit micropins. Compos A Appl Sci Manuf 156:106895. https://doi.org/10.1016/j.compositesa.2022.106895

12. Chang P, Mouritz AP, Cox BN (2006) Properties and failure mechanisms of z-pinned laminates in monotonic and cyclic tension. Compos Part A Appl Sci Manuf 37:1501–1513. https://doi.org/10.1016/j.compositesa.2005.11.013

13. Raimondi L, Tomesani L, Donati L, Zucchelli A (2021) Lattice material infiltration for hybrid metal-composite joints: manufacturing and static strenght. Compos Struct 269:114069. https://doi.org/10.1016/j.compstruct.2021.114069

14. Wang J, O'Gara JF, Tucker CL (2008) An objective model for slow orientation kinetics in concentrated fiber suspensions: theory and rheological evidence. J Rheol (N Y N Y) 52:1179–1200. https://doi.org/10.1122/1.2946437

15. Phelps JH, Tucker CL (2009) An anisotropic rotary diffusion model for fiber orientation in short- and long-fiber thermoplastics. J Nonnewton Fluid Mech 156:165–176. https://doi.org/10.1016/j.jnnfm.2008.08.002

16. Tseng H-C, Chang R-Y, Hsu C-H (2013) Method and computer readable media for determining orientation of fibers in a fluid. US Patent No. 8,571,828

17. Folgar F, Tucker CL (1984) Orientation behavior of fibers in concentrated suspensions. J Reinf Plast Compos 3:98–119. https://doi.org/10.1177/073168448400300201

18. Oubellaouch K, Pelaccia R, Bonato N et al (2024) Assessment of fiber orientation models predictability by comparison with X-ray μCT data in injection-molded short glass fiber-reinforced polyamide. Int J Adv Manuf Technol 130:4479–4492. https://doi.org/10.1007/s00170-024-12990-5

19. Tseng H-C, Chang RY, Hsu C-H (2018) Numerical Predictions of Fiber Orientation for Injection Molded Rectangle Plate and Tensile Bar with Experimental Validations. Int Polym Process 33(1):96–105. https://doi.org/10.3139/217.3404

20. Wang J, Jin X (2010) Comparison of recent fiber orientation models in autodesk moldflow insight simulations with measured fiber orientation data. Polym Process Soc 26th Annu Meet Banff Canada

21. Kuhn C (2018) Analysis and prediction of fiber matrix separation during compression molding of fiber reinforced plastics. Diss. Friedrich-Alexander-Universität Erlangen-Nürnberg (FAU)

22. Yamamoto S, Matsuoka T (1993) A method for dynamic simulation of rigid and flexible fibers in a flow field. J Chem Phys 98:644–650. https://doi.org/10.1063/1.464607

23. Yamamoto S, Matsuoka T (1995) Dynamic simulation of fiber suspensions in shear flow. J Chem Phys 102:2254–2260. https://doi.org/10.1063/1.468746

24. Joung CG, Phan-Thien N, Fan XJ (2001) Direct simulations of flexible fibers. J Nonnewton Fluid Mech 99:1–36. https://doi.org/10.1016/S0377-0257(01)00113-6

25. Switzer LH, Klingenberg DJ (2003) Rheology of sheared flexible fiber suspensions via fiber-level simulations. J Rheol (N Y N Y) 47:759–778. https://doi.org/10.1122/1.1566034

26. Qi D (2006) Direct simulations of flexible cylindrical fiber suspensions in finite Reynolds number flows. J Chem Phys 125(11):114901. https://doi.org/10.1063/1.2336777

27. Lindström SB, Uesaka T (2007) Simulation of the motion of flexible fibers in viscous fluid flow. Phys Fluids 19(11):113307. https://doi.org/10.1063/1.2778937

28. Kuhn C, Walter I, Täger O, Osswald T (2018) Simulative prediction of fiber-matrix separation in rib filling during compression molding using a direct fiber simulation. J Compos Sci 2(1):2.https://doi.org/10.3390/jcs2010002

29. Parkes PN, Butler R, Meyer J, de Oliveira A (2014) Static strength of metal-composite joints with penetrative reinforcement. Compos Struct 118:250–256. https://doi.org/10.1016/j.compstruct.2014.07.019

30. Summa J, Becker M, Grossmann F, Pohl M, Stommel M, Herrmann HG (2018) Fracture analysis of a metal to CFRP hybrid with thermoplastic interlayers for interfacial stress relaxation using in situ thermography. Compos Struct 193:19–28. https://doi.org/10.1016/j.compstruct.2018.03.013

31. Jansson A, Pejryd L (2019) Dual-energy computed tomography investigation of additive manufacturing aluminium–carbon-fibre composite joints. Heliyon 5:e01200. https://doi.org/10.1016/j.heliyon.2019.e01200

32. Stelzer PS, Cakmak U, Eisner L, Doppelbauer LK, Kallai´ I, Schweizer G, Prammer HK, Major Z (2022) Experimental feasibility and environmental impacts of compression molded discontinuous carbon fiber composites with opportunities for circular economy. Compos B Eng 234:109638. https://doi.org/10.1016/j.compositesb.2022.109638

33. Microsoft, Image Composite Editor (2016) http://research.microsoft.com/en-us/um/redmond/projects/ice/

34. Andrade ENDC (1930) The viscosity of liquids. Nature 125:580–4.https://doi.org/10.1038/125582a0

35. Sensini A, Pisaneschi G, Cocchi D, Kao A, Tozzi G, Zucchelli A (2022) High-resolution X-ray tomographic workflow to investigate the stress distribution in vitreous enamel steels. J Microsc 285:144–155. https://doi.org/10.1111/jmi.12996

36. Dantzig J, Tucker CL (2001) Modeling in materials processing. Cambridge University Press, New York

37. Castro JM, Macosko CW (1980) Kinetics and rheology of typical polyurethane reaction injection molding systems. Society of Plastics Engineers (Technical Papers), pp 434–438

38. Castro JM, Macosko CW (1982) Studies of mold filling and curing in the reaction injection molding process. AIChE J 28:250–260. https://doi.org/10.1002/aic.690280213

39. Cross MM (1965) Rheology of non-Newtonian fluids: a new flow equation for pseudoplastic systems. J Colloid Sci 20:417–437. https://doi.org/10.1016/0095-8522(65)90022-X

40. Teuwsen J, Hohn SK, Osswald TA (2020) Direct fiber simulation of a compression molded ribbed structure made of a sheet molding compound with randomly oriented carbon/epoxy prepreg strands—A comparison of predicted fiber orientations with computed tomography analyses. J Compos Sci 4(4):164.https://doi.org/10.3390/jcs4040164

41. Garschke C, Parlevliet PP, Weimer C, Fox BL (2013) Cure kinetics and viscosity modelling of a high-performance epoxy resin film. Polym Test 32:150–157. https://doi.org/10.1016/j.polymertesting.2012.09.011

42. Kamal MR, Sourour S (1973) Kinetics and thermal characterization of thermoset cure. Polym Eng Sci 13:59–64. https://doi.org/10.1002/pen.760130110

43. Wan Y, Straumit I, Takahashi J, Lomov SV (2018) Micro-CT analysis of the orientation unevenness in randomly chopped strand composites in relation to the strand length. Compos Struct 206:865–875. https://doi.org/10.1016/j.compstruct.2018.09.002

Publisher's Note Springer Nature remains neutral with regard to jurisdictional claims in published maps and institutional affiliations.